Computational Study of a Generic T-tail Transport

S. Naomi McMillin*, Neal T. Frink†, Patrick C. Murphy‡, Kevin Cunningham§, and Gautam H. Shah¶
NASA Langley Research Center, Hampton, VA, 23681-2199

Sudheer N. Nayani‖
Analytical Services & Materials, Inc., Hampton, VA, 23666

This paper presents a computational study on the static and dynamic stability characteristics of a generic transport T-tail configuration under a NASA research program to improve stall models for civil transports. The NASA Tetrahedral Unstructured Software System (TetrUSS) was used to obtain both static and periodic dynamic solutions at low speed conditions for three Reynolds number conditions up to 60 deg angle of attack. The computational results are compared to experimental data. The dominant effects of Reynolds number for the static conditions were found to occur in the stall region. The pitch and roll damping coefficients compared well to experimental results up to up to 40 deg angle of attack whereas yaw damping coefficient agreed only up to 20 deg angle of attack.

Nomenclature

b	=	wing span, ft
C_D	=	drag coefficient, 2(drag) /$\rho_\infty U_\infty^2 S$
C_L	=	lift coefficient, 2(lift) /$\rho_\infty U_\infty^2 S$
C_l	=	rolling moment coefficient, 2(rolling moment) /$\rho_\infty U_\infty^2 Sb$
$C_{l,p}$	=	roll damping coefficient
C_m	=	pitching moment coefficient, 2(pitching moment) /$\rho_\infty U_\infty^2 S\overline{c}$
$C_{m,q}$	=	pitch damping coefficient
C_n	=	yawing moment coefficient, 2(yawing moment) /$\rho_\infty U_\infty^2 Sb$
$C_{n,r}$	=	yaw damping coefficient
C_p or Cp	=	surface pressure coefficient, $2(P - P\infty)/(\rho_\infty U_\infty^2 S)$
C_Y	=	side force coefficient, 2(side force) /$\rho_\infty U_\infty^2 S$
$\overline{c}$	=	mean aerodynamic chord, ft
f	=	frequency, Hz
k_P	=	reduced frequency for pitch oscillation, $\pi f\overline{c}/U_\infty$
k_R, k_Y	=	reduced frequency for roll and yaw oscillation, $\pi fb/U_\infty$
L	=	fuselage length, ft
M_∞	=	free-stream Mach number
MRC	=	moment reference center, ft
P	=	local pressure, lb/ft^2
P_∞	=	free-stream pressure, lb/ft^2
rate1, *rate2*	=	volume grid spacing parameters in VGRID
$Re_{\overline{c}}$ or Re_c	=	Reynolds number based on mean aerodynamic chord
S	=	wing area, ft^2
U_∞	=	free-stream velocity, ft/s
X	=	streamwise coordinate for USM3D geometry, in.
Y	=	spanwise coordinate for USM3D geometry, in.

*Aerospace Engineer, Configuration Aerodynamics Branch,MS 499, AIAA Senior Member.
†Aerospace Engineer, Configuration Aerodynamics Branch, MS 499, Associate Fellow AIAA.
‡Senior Research Engineer, Dynamic Systems and Control Branch, MS 308, Associate Fellow AIAA.
§Senior Research Engineer, Flight Dynamics Branch, Mail Stop 308, Associate Fellow AIAA.
¶Senior Research Engineer, Flight Dynamics Branch, and Manager, TASA, MS 308, Associate Fellow AIAA.
‖CFD Manager, AS&M, 107 Research Drive, Associate Fellow AIAA.

$y+$ = non-dimensional wall distance
Z = vertical coordinate for USM3D geometry, in.

Symbols

α = angle of attack, deg
β = sideslip angle, deg
$\Delta n_1/\overline{c}$ = VGRID input parameter, initial spacing of viscous grid layer nondimensionalized by $\overline{c}$
Δt = physical time step, seconds
$\Delta t*$ = characteristic time step, $\Delta t U_\infty/\overline{c}$
$\Delta\alpha$ = pitch perturbation angle for F-O about the Y axis, deg
$\Delta\varphi$ = roll perturbation angle for F-O about the X axis, deg
$\Delta\psi$ = yaw perturbation angle for F-O about the Z axis, deg
ρ_∞ = free-stream density

Key Acronyms

12-Ft LST = NASA Langley Research Center 12-Foot Low-Speed Tunnel
AFM = advancing front method
CFD = Computational Fluid Dynamics
F-O = forced oscillation
FVWT = Boeing Flow Visualization Water Tunnel
GTT = generic T-tail
NAART = Boeing North American Aviation Research Tunnel
RANS = Reynolds-averaged Navier-Stokes
SA = Spalart-Allmaras one-equation turbulence model
SST = Menter Shear Stress Transport two-equation turbulence model
TASA = Technologies for Airplane State Awareness
TetrUSS = Tetrahedral Unstructured Software System
TER, TEL = trailing edge right, trailer edge left
TEU, TED = trailing edge up, trailing edge down

I. Introduction

NASA is conducting research on how to improve the stall models for civil transports in motion-based flight simulators [1–4] in support of a pending Federal Aviation Administration requirement [5] that enhanced flight simulator models be implemented by early 2019 for training pilots to recognize precursors to stall and to learn upset recovery strategies. While the majority of this research has relied on experimental data sources, a portion has been dedicated to exploring ways to infuse computational aerodynamic data into the stall models [6]. High fidelity computational fluid dynamics (CFD) tools offer the potential to approximate increments for ground-to-flight scaling effects, as well as to augment the dynamic damping derivative data for the simulators.

NASA and Boeing Research and Technology have partnered to conduct a series of wind-tunnel tests for a generic T-tail (GTT) regional jet configuration as part of research and development of advanced modeling and uncertainty quantification methods for flight dynamics [7]. From this, a motion-based flight simulator model has been developed for assessing its flight characteristics into stall [8]. This paper describes additional data computed for the GTT from the Tetrahedral Unstructured Software System (TetrUSS) [9] to provide overall increments for Reynolds number effect and to augment the stalled portion of the flight simulator model with dynamic damping derivatives as described in Ref.[10, 11].

II. Geometry Description

The generic T-tail configuration used in this work was derived from a remotely piloted airplane configuration that was designed by NASA and Area-I, Inc. The design was intended to be a 15.8% scaled model of a generic short to medium range twin-jet transport with aft mounted engines and a T-tail. The remotely piloted vehicle was built by Area-I [12] and delivered to NASA for use in loss-of-control-prevention research [13] being conducted under the NASA Aviation Safety Program. Due to NASA programmatic replanning, that vehicle was not flown. A modified variant of the remotely piloted airplane design was used as the basis for a theoretical full scale configuration and the wind tunnel models.

The full scale airplane aerodynamic reference geometry is shown in Table 1 and the scale factors (relative to full scale) for the wind tunnel models and computational model are shown in Table 2. The GTT configuration geometry and control layout is shown in Fig. 1. The moment reference center (*MRC*) is located at the 25% mean aerodynamic chord location. A different model was constructed for each test to the maximum scale practical for each facility. The models used in these tests were constructed using inexpensive rapid prototyping construction techniques. The models for the NASA Langley Research Center 12-Foot Low-Speed Tunnel (12-Ft LST) and the the Boeing Flow Visualization Water Tunnel (FVWT) were both constructed using polycarbonate three dimensional printing techniques. The model used in the Boeing North American Aviation Research Tunnel (NAART) test was constructed using a stereo lithography process. Flow-through engine nacelles were used on all three models. Propulsion effects were not tested during these tunnel entries.

The models used in the 12-Ft LST and NAART tests were constructed with individual control surfaces parts so the effect of control surface deflections could be studied. Control surface deflection ranges are shown in Table 3. The flaps on the GTT configuration are plain flaps. The computational study presented here only examined the GTT configuration with flaps and control surfaces set to 0 deg.

III. Experiment Description

To stay within the constraints of budget, workforce, and schedule the TASA research has used a generic airplane model, focused on a single clean wing (flaps/slats up) configuration, and used low-cost tunnels. Tunnel tests were conducted in 12-Ft LST, FVWT, and NAART. As a result, the tunnel results were obtained at low-speed and low chord-based Reynolds number ($Re_{\bar{c}} \leq 270{,}000$). Across the three wind tunnel tests, static force and moment data, forced-oscillation force and moment data, and various types of flow visualization data were obtained. Reference [13] contains a detailed description of the wind tunnel tests conducted on the GTT configuration.

IV. Computational Methodology

The CFD computations were performed using the NASA Tetrahedral Unstructured Software System (TetrUSS) [9]. This system consists of loosely integrated, user-friendly software that comprises a geometry setup utility GridTool, a tetrahedral grid generator VGRID, a flow solver USM3D, and post-processing visualization and data extraction utilities.

A. Grid Generator

VGRID [14] [15] is a tetrahedral grid generator based on the advancing front method (AFM) for generation of surface triangles and "inviscid" field cells, and the advancing layers method (ALM) for generation of thin-layered "viscous" cells. Both techniques are based on marching processes in which tetrahedral cells grow from an initial front (triangular surface mesh) until the volume around the geometry is filled. Unlike the conventional AFM, which introduces cells into the field in a totally unstructured manner, the ALM generates organized layers of thin tetrahedral cells, one layer at a time, while maintaining the flexibility of AFM. Once the advancing front process is completed in VGRID, an additional postprocessing step is required using POSTGRID to close any open pockets and to improve grid quality. VGRID input files are generated by an interactive geometry manipulation program, GridTool. This graphics tool can import surface definitions from initial graphics exchange specification (IGES) files containing nonuniform rational B-spline surfaces and curves, as well as PLOT3D point definition files. GridTool is used to manipulate the geometry and to define necessary geometric surface patches and grid spacing (source) parameters.

B. Flow Solver

The computations are performed with USM3D [16], which is a parallelized tetrahedral cell-centered, finite volume Navier-Stokes flow solver. The term "cell centered" means that the finite volume flow solution is solved at the centroid of each tetrahedral cell. Inviscid flux quantities are computed across each tetrahedral cell face using various upwind schemes. Spatial discretization is accomplished by a novel reconstruction process, based on an analytical formulation for computing solution gradients within tetrahedral cells. The solution can be advanced in time by a 2nd-order "physical" time step scheme, a 2nd-order "dual" time step scheme, or to a steady-state condition by an implicit backward-Euler scheme. Several turbulence models are available: the Spalart-Allmaras (SA) one-equation model, the two-equation $k-\epsilon$ turbulence model, the Menter Shear Stress Transport (SST) two-equation model, and the nonlinear Algebraic Reynolds Stress Models of Girimaji and Shih/Zhu/Lumley. Detached Eddy Simulation (DES) has been implemented in all of the turbulence models, but has not been fully tested. Body motion is controlled by an internal sinusoidal motion generator. The latest extensions to the USM3D flow solver are described in Reference [17].

C. Solution Strategy

USM3D solutions were generated using an implicit second-order physical time-step scheme for both the static and dynamic cases. Inviscid fluxes are computed with Roe's flux difference scheme without limiting. The time-accurate Reynolds-averaged Navier-Stokes (RANS) flow solutions are primarily computed with the SA turbulence model. Limited assessments are also made for the static cases with the SST turbulence models. The boundary conditions consist of a surface no-slip constraint on the wing and characteristic inflow/outflow on the outer box. The forced oscillation (F-O) solutions are generated using nondeforming solid-body rotation of the full grid about the X, Y, or Z axis and initialized by restarting from a converged static solution at the prescribed angle of attack, α, and cycled for 1.5 sinusoidal oscillations. However, the hysteresis of forces and moments is converged to its periodic solution after the first half cycle of oscillation; only the subsequent full cycle is plotted in the correlation with experiment.

V. Grid Generation

Each tetrahedral grid used in this investigation was produced with an outer boundary box prescribed at minimum X, Y, Z of $-10L$ each, where L is the fuselage length, and maximum X, Y, Z of $10L$ each. The normal spacing for the grids was prescribed with the VGRID parameters as given in Table 4. The $\Delta n_1/\overline{c}$ is the VGRID input parameter defining the initial spacing of the viscous grid layer, where $\Delta n_1/\overline{c}$ is in grid units. The $y+$ parameter was used to determine $\Delta n_1/\overline{c}$ and is based on the boundary layer thickness which is calculated using the Reynolds number at the wing half-chord position.

Four grids were generated for the GTT configuration of Fig. 1. The grids varied in boundary layer thickness due to differing $Re_{\overline{c}}$ as seen in Table 4. Grids 1 and 2 were generated using $Re_{\overline{c}} = 0.27 \times 10^6$. Grids 3 and 4 were generated using $Re_{\overline{c}} = 1.6 \times 10^6$ and 16×10^6, respectively. The first step in creating a grid was to generate a half grid using the plane of symmetry as one of the boundaries of the grid. The half-span grid for the $Re_{\overline{c}} = 0.27 \times 10^6$ was used as Grid 1. Grid 1 was then mirrored to create a full grid which was used as Grid 2. The same process was used to generate full grids for the $Re_{\overline{c}} = 1.6 \times 10^6$ and 16×10^6 cases. The half-span grids used to generate the full grids for Grids 3 and 4 were not used in this investigation.

Grids 3 and 4 use the same surface grid which was coarser than that used for Grids 1 and 2 in an attempt to reduce grid size. The higher Reynolds number of Grids 3 and 4 would require a smaller $\Delta n_1/c$ which would drive up the volume grid size. The coarser surface grid would help mitigate the increase in volume grid size due to the smaller $\Delta n_1/c$ parameter needed for the increase in Reynolds number. Fig. 2 shows the surface grid used in Grids 3 and 4. Fig. 2a shows the entire upper surface grid for Grid 3 at an oblique view angle. Fig. 2b shows a close-up of the wing and Fig. 2c shows a close-up view of the nacelles and T-tail. Fig. 3 shows cross-sectional cuts of the volume grid at Y = 13.8 inches, and X = 110, 145, and 185 inches for Grid 3.

VI. Results

Static and dynamic USM3D force and moment coefficient data were computed for various combinations of free-stream Mach number (M_∞), $Re_{\overline{c}}$, α, perturbation angle, and reduced frequency on the GTT configuration. Table 5 contains the overall flow conditions and model orientation conditions for this investigation. First, the static solutions will be presented with a discussion of solution convergence and the sensitivities to time step, turbulence model, and Reynolds number. Then the forced-oscillation results will be analyzed within the context of creating dynamic damping

coefficients.

A. Static Solutions

1. Solution Convergence

Table 6 shows the 152 static cases obtained in this investigation. Static solutions were generated by running solutions using a characteristic time step (Δt^*) of 0.02 or 0.10. Solutions were obtained using either the SA or SST turbulence models. Each solution was run until the coefficients were converged. Both the lift coefficient, C_L, and pitching moment coefficient, C_m, were examined to determine convergence. Only the C_L convergence history will be presented here. Fig. 4 shows four examples of convergence observed in the solutions. Fig. 4a shows the steady convergence history of C_L for Grid 2 at $M_\infty = 0.126$, $\alpha = 10°$, and $Re_{\bar{c}} = 0.27 \times 10^6$. Increasing α by 1° results in an oscillating convergence history for C_L as seen in Fig. 4b. Evidence of periodic wake shedding is manifested in Fig. 4c - 4d for Grid 4 at the higher angles of attack, $\alpha = 16°$ and 17°, respectively, which are at the lower Reynolds number of 0.27×10^6. The larger amplitude of the oscillating convergence histories of Fig. 4c- 4d required an order-of-magnitude increase in the number of required time steps when compared to the steady convergence of Fig. 4a and the much smaller oscillating convergence (i.e. smaller amplitude) of Fig. 4d. The cases with an oscillating convergence in C_L are indicated by a star symbol in Table 6.

2. Effect of Characteristic Time Step

Static solutions were generated by running solutions using Δt^* of 0.02 or 0.10. Fig. 5 shows a comparison $\Delta t^* = 0.02$ and 0.10 on the C_L and C_m for Grid 2 at $M_\infty = 0.126$, $Re_{\bar{c}} = 0.27 \times 10^6$, and $6° \leq \alpha \leq 20°$ using the SA turbulence model. The error bars are the standard deviation of the coefficient variation over the integration interval from the convergence history of that coefficient. The error bars are significant for the cases where the coefficient history has an oscillation with a large amplitude. The data of Fig. 5 show that Δt^* has little effect on the aerodynamic coefficients. The same trend was observed on Grids 3 and 4 (data not presented here) and for the Grid 2 SST data as well (data not presented here).

3. Effect of Turbulence Model

Static solutions were generated by running solutions using either the SA one-equation model or the SST two-equation model. Fig. 6 shows a comparison of the SA and SST turbulence models for Grid 3 at $M_\infty = 0.126$, $Re_{\bar{c}} = 1.6 \times 10^6$, and $0° \leq \alpha \leq 20°$ using $\Delta t^* = 0.02$. Wind tunnel data from the NAART and 12-Ft LST tunnel tests on the GTT configuration are also shown in Fig. 6. The dominant effect of turbulence model occurs at wing stall. The SST solution predicts the stall occurring at $\alpha = 7°$ whereas the SA solution predicts stall at $\alpha = 9°$ as seen in the C_L data of Fig. 6a. Beyond stall, the predicted C_L for the SST turbulence model solution is lower than that of the SA turbulence model solution and experimental data as was observed in a previous guideline study of a similar subsonic transport airplane (see Ref. [18]). C_m and drag coefficient (C_D) data (Fig. 6b and Fig. 6c) show the SST turbulence model solution underpredicting C_m and C_D at $\alpha > 14°$. No lateral-directional asymmetries were present in the solutions computed at zero degrees sideslip (data not presented here).

4. Effect of Reynolds Number

Fig. 7 shows the effect of Reynolds number on aerodynamic coefficients at $0° \leq \alpha \leq 20°$. Fig. 8 shows the same at $20° \leq \alpha \leq 60°$. The low-speed wind tunnel data from the 12-Ft LST and the NAART wind tunnel are also shown in Fig. 7 and Fig. 8. The dominant effects of $Re_{\bar{c}}$ is within the stall region ($8° \leq \alpha \leq 20°$) as seen in Fig. 7. The impact of $Re_{\bar{c}}$ on C_L and C_m away from the stall region (i.e., $\alpha > 20°$) is nearly constant as seen in Fig. 8. CFD-derived increments due to Reynolds number have been added to the low-Reynolds number simulator data as a ground-to-flight correction. The impact of these corrections is being evaluated in piloted simulations [8].

As stated above, the dominant effects of $Re_{\bar{c}}$ is within the stall region ($8° \leq \alpha \leq 20°$). The C_L and C_m data of Fig. 7a and 7a show three breaks in the data curve slopes for $\alpha < 20°$. An increase in $Re_{\bar{c}}$ increases the α condition at which these breaks occur as shown in Table 7. The first break in the C_L curve corresponds to separation occurring on the outboard wing as seen in the streamline data of Fig. 9. Fig. 9 presents surface pressure coefficient (C_p) and streamline data over the left wing at $\alpha = 9°$ and 10° for $M_\infty = 0.126$ and $Re_{\bar{c}} = 1.6 \times 10^6$. The red streamline data were obtained on Y-constant planes of -13.8, 22, 31, 38, 45, 52, 59, and 66 inches. The green ribbon streamline data were obtained by

seeding a point near the vortex core on the $Y = 13.8$ inch plane. The purple ribbon streamline data were obtained by seeding a point near the vortex core on the $Y = 66$ inch plane. Both the $\alpha = 9°$ and $10°$ solutions show a flow separation occurring at the wing/body juncture. However, only the $\alpha = 10°$ data of Fig. 9b shows a vortex occurring on the outboard wing.

The second and third breaks identified correspond to significant changes in the separation occurring near the body/wing juncture. Fig. 10 presents streamline data occurring at $\alpha = 13°$ and $14°$ for $M_\infty = 0.126$ and $Re_{\bar{c}} = 1.6 \times 10^6$. The separation on the most inboard part of the wing decreases drastically going from $\alpha = 13°$ and $14°$ where the second break in the C_L and C_m vs α curves occurs. The opposite trend is true at the third break as seen in the streamline data occurring at $\alpha = 18°$ and $19°$ for $M_\infty = 0.126$ and $Re_{\bar{c}} = 1.6 \times 10^6$ (Fig. 11).

B. Dynamic Solutions

The dynamic stability and control USM3D contributions to the GTT flight simulation database have been produced by mimicking the experimental approach of forced sinusoidal motion about roll, pitch, and yaw axes. A dynamic USM3D solution was obtained by restarting a converged static solution at the desired M_∞, $Re_{\bar{c}}$, and α conditions and moving the grid in a sinusoidal oscillation cycle about the desired axes. The perturbation angles of the pitch, roll, and yaw forced-oscillation (F-O) solutions were 5°, 10°, and 10°, respectively. Table 8 shows the 72 cases obtained on Grid 1 and Table 9 shows the 38 cases obtained on Grid 2 and 23 cases obtained on Grid 4.

1. Solution Steadiness

Typically, a periodic dynamic solution was obtained within 1.5 cycles. The first 0.5 cycle was discarded due to transient flow conditions in the start-up of the dynamic solution. The remaining cycle was used in subsequent analyses. Angle of attack and $Re_{\bar{c}}$ affected the steadiness of the hysteresis loops. Fig. 12 shows USM3D rolling moment coefficient (C_l) hysteresis loops for $\alpha = 8°$ and $22°$ for $M_\infty = 0.27$, $Re_{\bar{c}} = 16 \times 10^6$, and $k_R = 0.0940$. Even though both of the static solutions at $\alpha = 8°$ and $22°$ for $Re_{\bar{c}} = 16 \times 10^6$ were steady, the steadiness of the dynamic solutions between the two angles of attack are very different. At $\alpha = 22°$, the hysteresis was exactly repeated in the second cycle. However, at $\alpha = 8°$, the hysteresis loop is not steady between the three cycles of the dynamic USM3D solution. Fig. 13 shows the effect of $Re_{\bar{c}}$ on the USM3D C_l hysteresis loops for $\alpha = 8°$ for $M_\infty = 0.27$, $Re_{\bar{c}} = 0.27 \times 10^6$ and 16×10^6, and $k_R = 0.0940$. The hysteresis loops for the lower $Re_{\bar{c}}$ are steady between cycles 1 and 2, whereas the higher $Re_{\bar{c}}$ solution has unsteady hysteresis loops between the three cycles.

2. Damping Coefficients

Fig. 14 depicts a comparison of computed and experimentally measured C_m from pitch F-O data at $0° \leq \alpha \leq 60°$, $k_P = 0.0158$, and low $Re_{\bar{c}}$. The top plot of Fig. 14 shows experimental pitch F-O data from the 12-Ft LST while the bottom plot shows similar USM3D data. The static USM3D C_m has been shifted by 0.2 to better align the data for visual correlation. This shift is due to C_m being referenced to different longitudinal stations. However, for dynamic stability, the shape and size of the hysteresis loops are the important characteristics. Fig. 14 shows a very good visual correlation. This good correlation is quantified in the pitch damping coefficient ($C_{m,q}$) in Fig. 15 where reasonable agreement is observed up to $\alpha = 40°$.

The effect of $Re_{\bar{c}}$ on the roll damping coefficient ($C_{l,p}$) is shown in Fig. 16. The USM3D and 12-Ft LST data were obtained at $0° \leq \alpha \leq 60°$ and $k_R = 0.0158$. The USM3D data were obtained at $Re_{\bar{c}} = 0.27 \times 10^6$ and 16×10^6. The effect of $Re_{\bar{c}}$ on the USM3D data is small at the lower and higher angles of attack but shows significant variation at $8° \leq \alpha \leq 14°$ where highly unsteady shedding of wakes were observed in flow visualizations from the wind-tunnel test. Additional analysis is needed to assess whether these differences are due to $Re_{\bar{c}}$ or from the randomness of the wake shedding.

The effect of frequency on the yaw damping coefficient ($C_{n,r}$) is shown in Fig. 17 at $0° \leq \alpha \leq 60°$ and low $Re_{\bar{c}}$, and $k_Y = 0.047$, 0.094, and 0.188. The frequency effect in the USM3D data is negligible up to $\alpha = 30°$. This observation corresponds to the FVWT data but only to 20°. The USM3D $C_{n,r}$ coefficients are generally within the 2σ bounds of the 12-Ft LST data.

VII. Summary

A computational study has been presented using a generic transport T-tail (GTT) configuration to develop a data set for use in research into flight dynamics of this type of aircraft. The computational solutions occurred at Mach numbers

of 0.126 and 0.27, Reynolds numbers of 0.27×10^6, 1.6×10^6, and 16×10^6, and angles of attack from -4° to 60°. The computational solutions were compared with wind-tunnel data obtained in the NASA Langley Research Center 12-Foot Low-Speed Tunnel, the Boeing North American Aviation Research Tunnel, and the Boeing Flow Visualization Water Tunnel.

Best practices from previous work on a different T-tail geometry were utilized in setting up the computational study. Brief parametric studies were conducted to solidify the choice of time step, turbulence model and convergence criteria. The majority of the static solutions were used in examining the effect of Reynolds number on the aerodynamics of the GTT configuration. These static solutions were then used to start the periodic dynamic solutions.

The dominant effects of Reynolds number were found to occur in the stall region for the GTT configuration. The breaks in the lift coefficient vs angle of attack and pitching moment coefficient vs angle of attack curves due to wing stall were affected dramatically and were delayed to higher angles of attack with increasing Reynolds number. Flow visualization was used to illustrate the wing flow leading up to and including stall conditions.

Damping coefficients for the GTT configuration were obtained using the periodic solutions and compared to wind-tunnel test results. The pitch and roll damping coefficients compared well to experimental results up to an angle of attack of 40° whereas yaw damping coefficient agreed only up to angle of attack of 20°.

Table 1 Full-scale aerodynamic reference dimensions.

Aerodynamic Reference	Symbol	Full Scale Dimension
Mean Aerodynamic Chord	$\overline{c}$	11.07 ft
Fuselage Length	L	98.19 ft
Wing Span	b	75.98 ft
Wing Area	S	754.32 ft^2

Table 2 Scale factors of test facility models.

Data Source	Model Scale Factor
NASA 12-Ft LST	0.057
Boeing NAART	0.020
Boeing FVWT	0.019
USM3D	0.16

Table 3 Control surface deflection ranges.

Control Surface	Deflection Range, degrees
Elevator	-20 (TEU) to +20 (TED)
Stabilizer	-10 (TEU) to +5 (TED)
Spoilers	0 to 60 (TEU)
Ailerons	-25 (TEU) to + 25 (TED)
Rudder	-30 (TER) to + 30 (TEL)
Flaps	0 to 60 (TED)

Table 4 Grid parameters.

Grid Name	Grid Type	$Re_{\overline{c}}$	Surface Cells	Volume Cells	$\Delta n_1/\overline{c}$	*rate1*	*rate2*	$y-plus$
Grid 1	Half-span	0.27×10^6	415,526	28,758,575	$0.14\times10^{-}3$	0.15	0.02	0.5
Grid 2	Full -span	0.27×10^6	831,052	57,517,150	$0.14\times10^{-}3$	0.15	0.02	0.5
Grid 3	Full-span	1.6×10^6	486,864	38,82,3976	$0.29\times10^{-}3$	0.15	0.02	0.5
Grid 4	Full-span	16×10^6	486,864	48,498,412	$0.36\times10-3$	0.15	0.02	0.5

Table 5 CFD study flow conditions.

Grid Name	Half-span Grid 1	Full-span Grid 2	Full-span Grid 3	Full-span Grid 4
$Re_{\bar{c}}$	0.27×10^6	0.27×10^6	1.6×10^6	16×10^6
M_∞	0.27	0.27	0.126	0.126
α	-4° to 60°			
β	0°			
Turbulence Model	SA, SST			
Pitch F-O				
Amplitude	5°	5°		5°
k_P	0.0015, 0.0025, 0.0041, 0.0060, 0.0079, 0.0120, 0.0158, 0.0200, 0.0250, 0.0316, 0.0400	0.0158		0.0158
Roll F-O				
Amplitude		10°		10°
k_R		0.094		0.094
Yaw F-O				
Amplitude		10°		
k_Y		0.047, 0.94, 0.188		

Table 6 Log for static CFD cases.

Grid Name	Half-span Grid 1	Full-span Grid 2		Full-span Grid 3				Full-span Grid 4	
M_∞	0.126	0.126		0.126				0.27	
$Re_{\bar{c}}$	0.27×10^6	0.27×10^6		1.6×10^6				16×10^6	
Δt^*	0.1	0.02	0.1	0.02	0.02	0.1	0.1	0.02	0.1
Turbulence Model	SA	SA	SA	SA	SST	SA	SST	SA	SA
α, deg									
-4	●		●						
0			●	●	●	●	●		●
2			●	●	●	●			●
4	●		●	●	●	●	●		●
6			●	●	●	●			●
8	●	●	●	●	●	●	●	●	●
9		★	●	★	●			●	●
10	●	★	●	★	●	●	●	●	●
11			★	★	●	★	●	●	●
12	★	★	●	★	●	★	●	●	●
13			★	★					●
14		★	★	★	★	●	★	●	●
15			★	★		★		●	●
16	●	●	●	★	●	★	●	★	★
17			●	★				★	★
18	●		●	●		●		●	★
19			●	●				●	●
20	●		●	●	●	●	●		●
22	●		●	●					●
24			●	●					●
26	●		●	●					●
28	●		●	●					●
30	●		●	●					●
35	●		●	●					●
40	●		●	●					●
45			●	●					●
50	●		●	●					●
55			●	●					●
60	●		●	●					●
	● -Steady Convergence; ★ - Oscillating Convergence								

Table 7 α conditions for breaks in the C_L and C_m vs α curves in Fig. 7.

$Re_{\bar{c}}$	1st Break	2nd Break	3rd Break
0.27×10^6	$8° < \alpha < 10°$	$12° < \alpha < 13°$	$15° < \alpha < 16°$
1.6×10^6	$9° < \alpha < 10°$	$13° < \alpha < 14°$	$18° < \alpha < 19°$
16×10^6	$9° < \alpha < 10°$	$15° < \alpha < 16°$	$18° < \alpha < 19°$

Table 8 Log for force-oscillation CFD cases on the half-span Grid 1.

Grid Name	Half-span Grid 1						
M_∞	0.126						
$Re_{\bar{c}}$	0.27×10^6						
Turbulence Model	SA						
Oscillation Type	Pitch						
k_P	0.0079	0.0120	0.0158	0.0200	0.0250	0.0316	0.0400
α, deg	$\Delta\alpha = \pm 5$						
-4			●				
0							
4			●	●			●
6							
8			●	●			●
10	●	●	●	●	●	●	●
12	●	●	●	●	●	●	●
14	●	●	●	●	●	●	●
16	●*See note	●	●	●	●	●	●
18	●	●	●	●	●	●	●
20	●	●	●	●	●	●	●
22	●	●	●	●	●	●	●
24				●			●
26							
28			●	●			●
30				●			●
35			●	●			●
40			●	●			●
45							
50			●				
55							
60			●				
*Note: Additional k_P = 0.0015, 0.0025, 0.0041, 0.0060							

Table 9 Log for force-oscillation CFD cases for full-span Grid 2 and Grid 4.

Grid Name	Full-span Grid 2					Full-span Grid 4	
M_∞	0.126					0.27	
$Re_{\bar{c}}$	0.27×10^6					16×10^6	
Turbulence Model	SA						
Oscillation Type	Pitch	Yaw			Roll	Pitch	Roll
Reduced Frequency	k_P = 0.0158	k_Y = 0.0470	k_Y = 0.0940	k_Y = 0.1880	k_R = 0.0940	k_P = 0.0158	k_R = 0.094
α, deg	$\Delta\alpha = \pm 5$	$\Delta\psi = \pm 10$			$\Delta\varphi = \pm 10$	$\Delta\alpha = \pm 5$	$\Delta\varphi = \pm 10$
-4			●				
0	●				●	●	●
4	●		●		●	●	●
6					●		●
8	●		●		●	●	●
10					●	●	●
12			●		●	●	●
14					●	●	●
16			●		●	●	●
18					●	●	●
20			●		●	●	●
22					●	●	●
24					●	●	●
26			●				
28							
30		●	●	●			
35		●	●	●			
40		●	●	●			
45		●	●	●			
50		●	●	●			
55							
60			●				

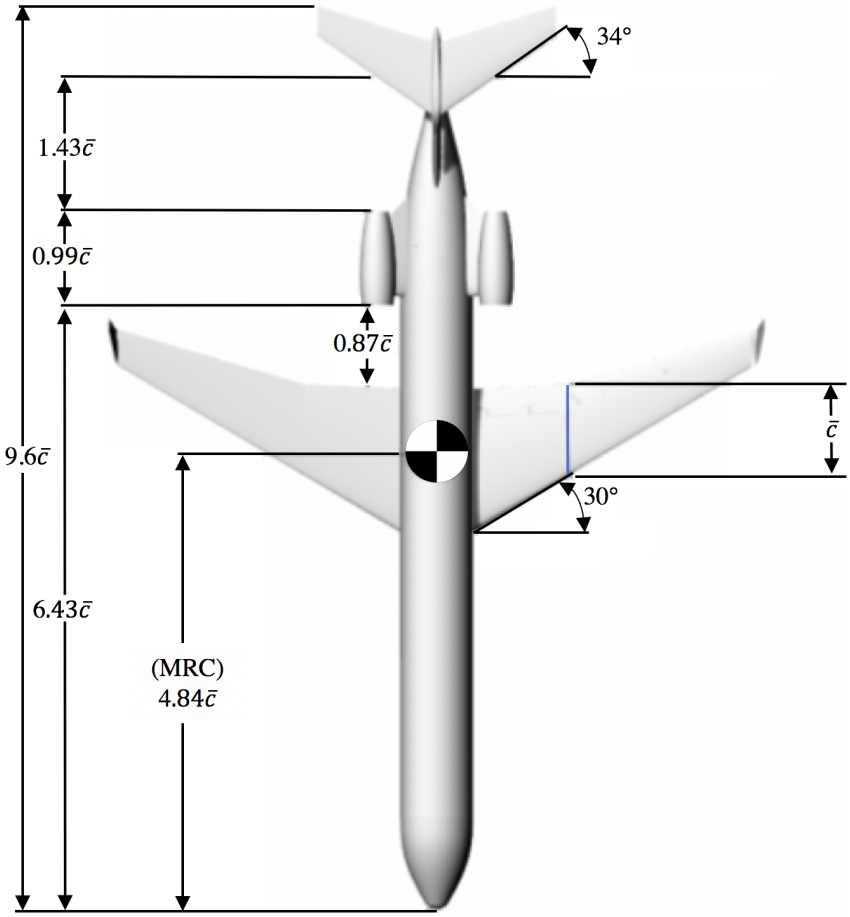

(a) Dimensional drawing shown in the plan view.

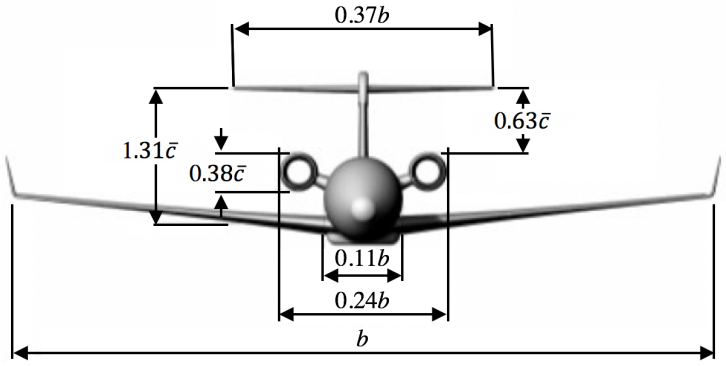

(b) Dimensional drawing is shown from a front perspective.

Fig. 1 Sketches of the GTT configuration.

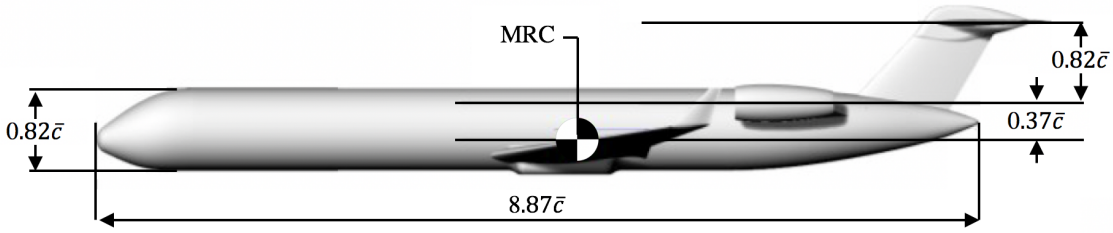

(c) Dimensional drawing is shown from a left side perspective.

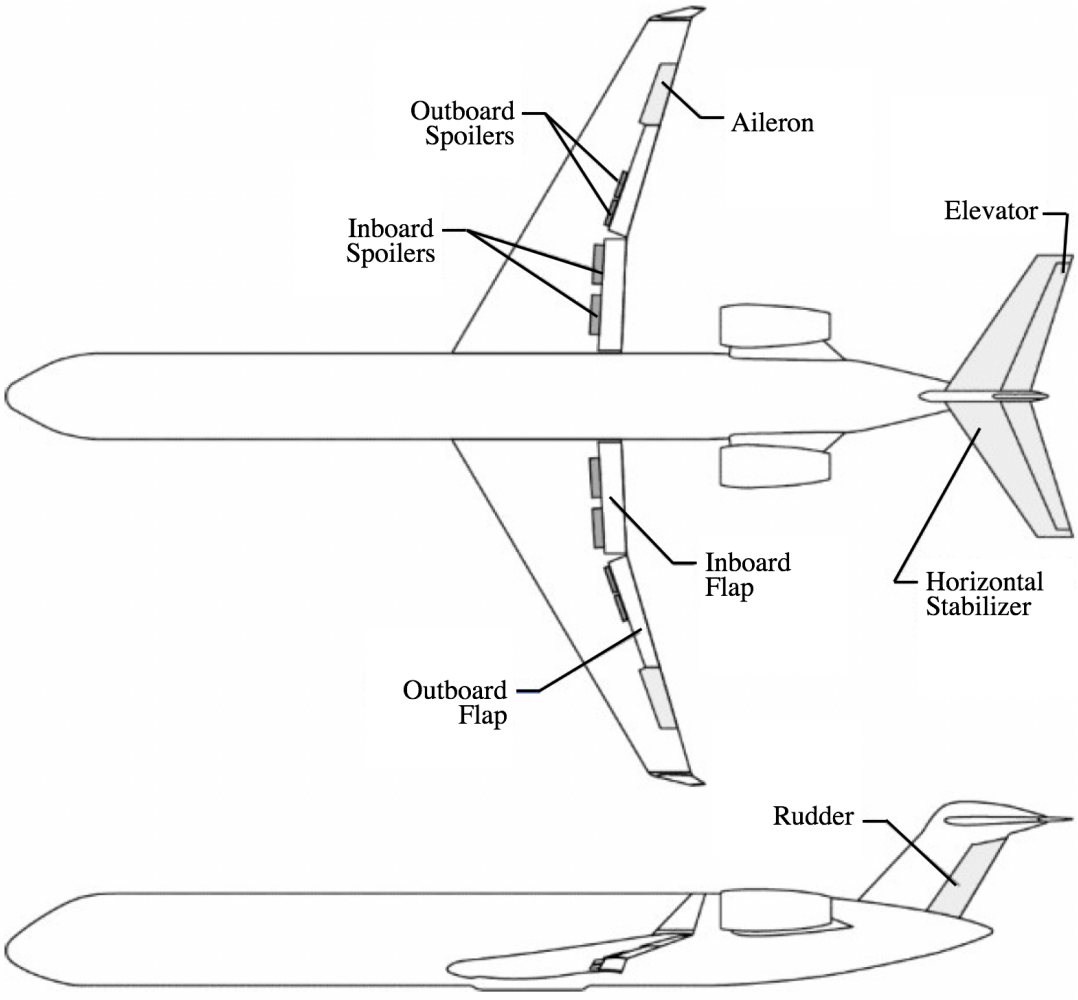

(d) Sketch showing control surface arrangement.

Fig. 1 Concluded.

(a) Oblique top view.

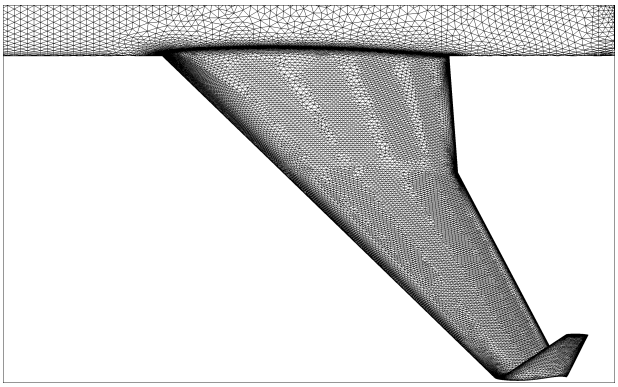

(b) Wing at 50° roll angle

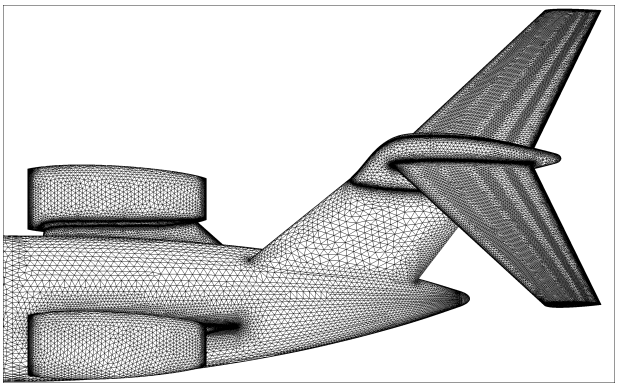

(c) Nacelles and T-tail at 50° roll angle.

Fig. 2 Views of the surface grid used in Grids 3 and 4.

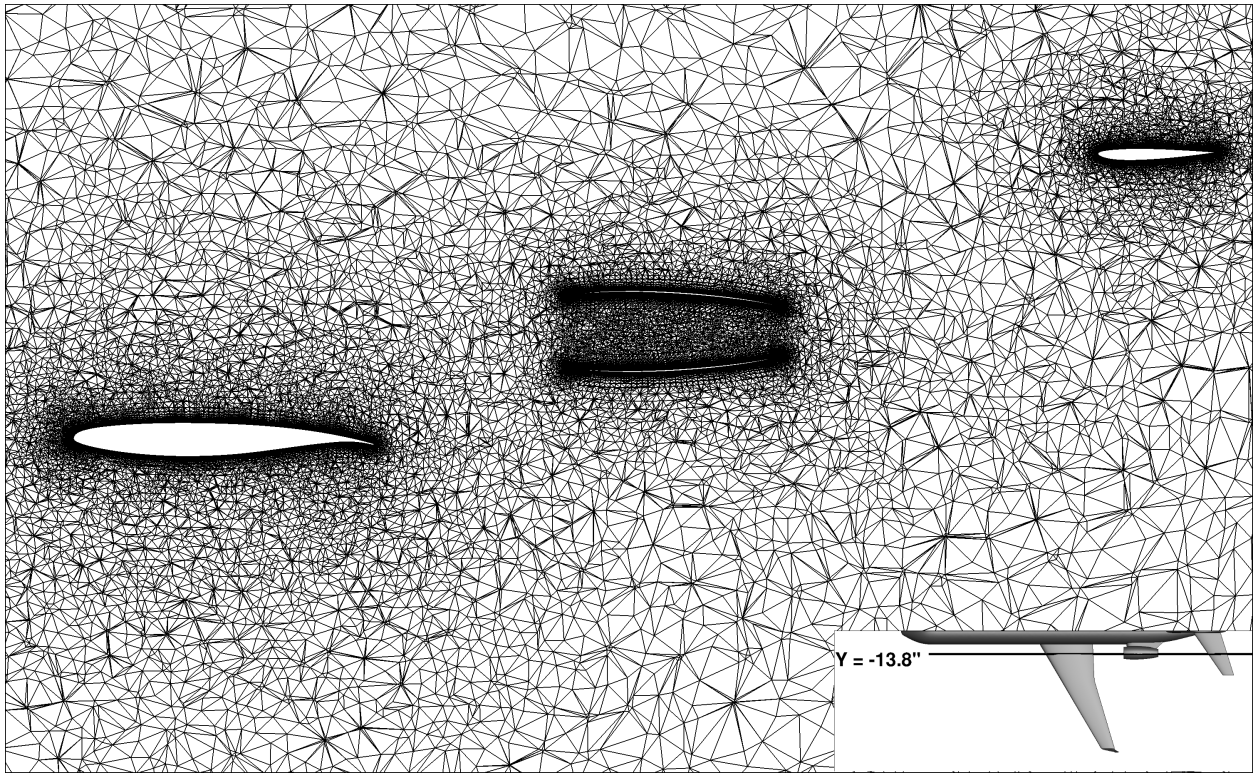

(a) Y = 13.8 inches.

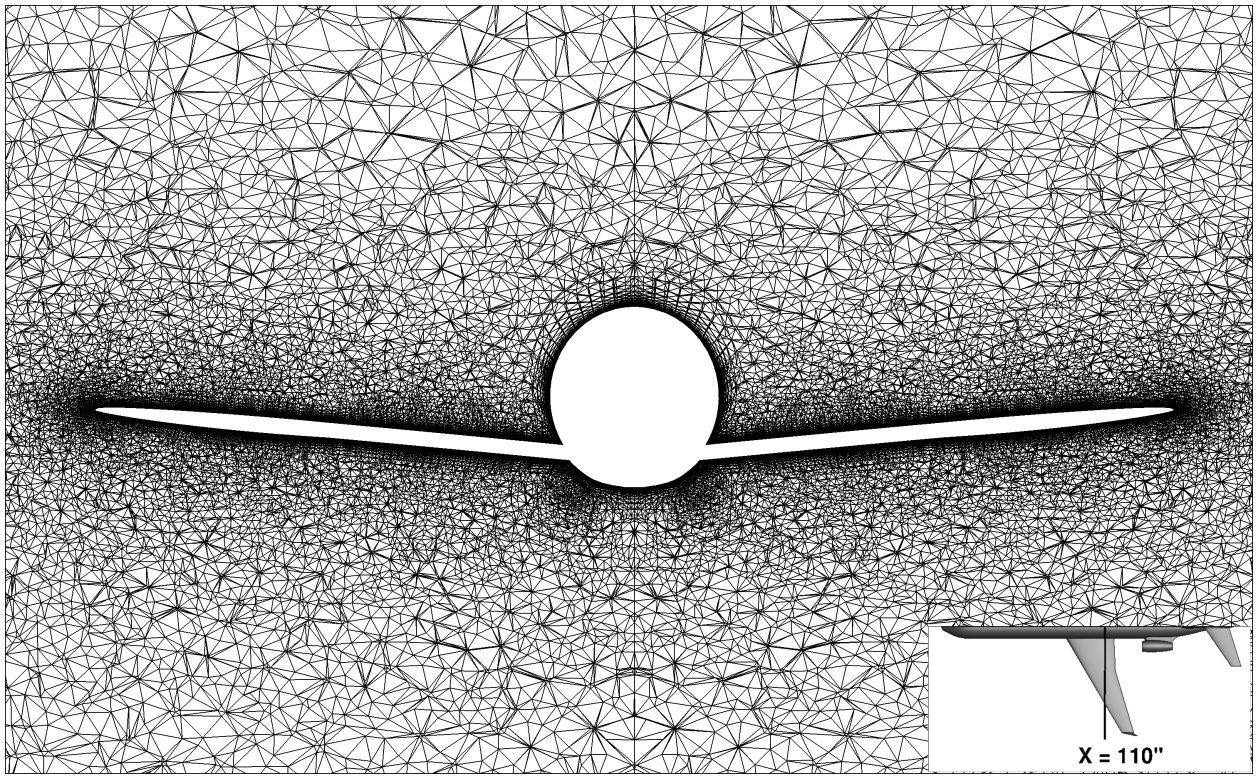

(b) X = 110 inches.

Fig. 3 Cross-sectional cuts of the volume grid for Grid 3.

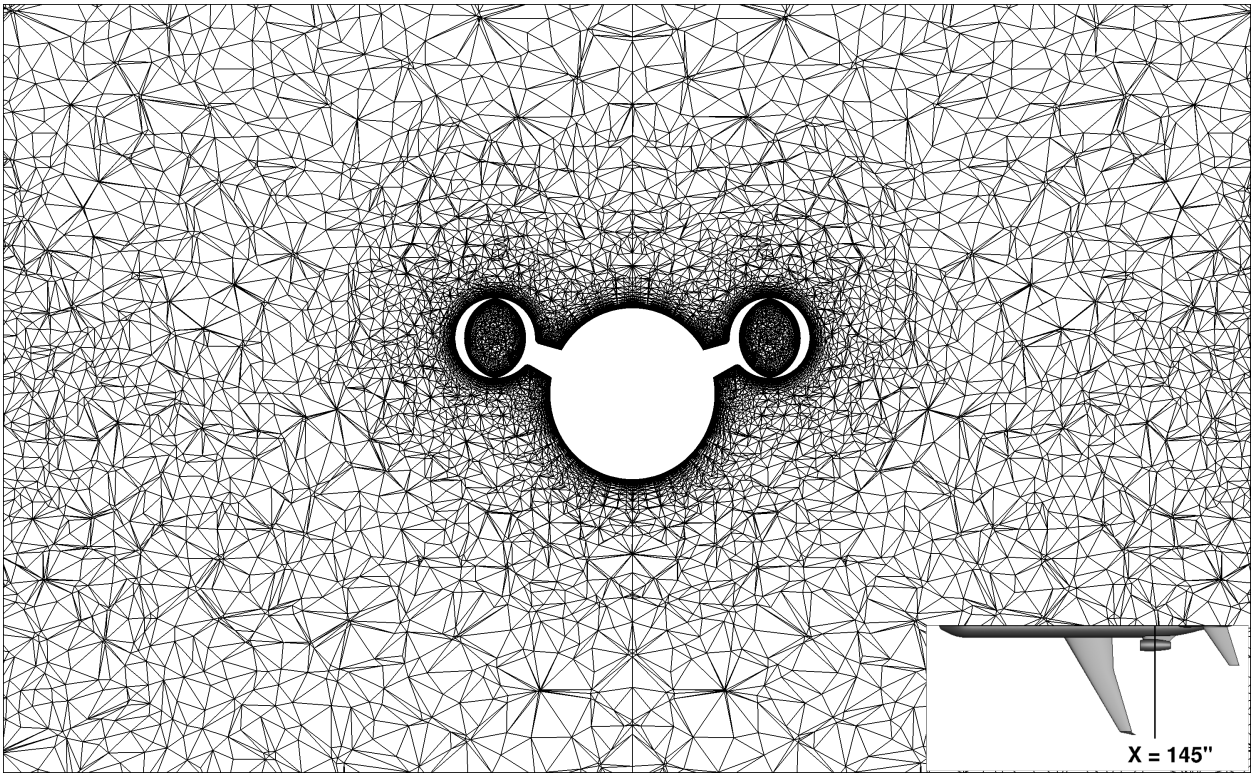

(c) X = 145 inches.

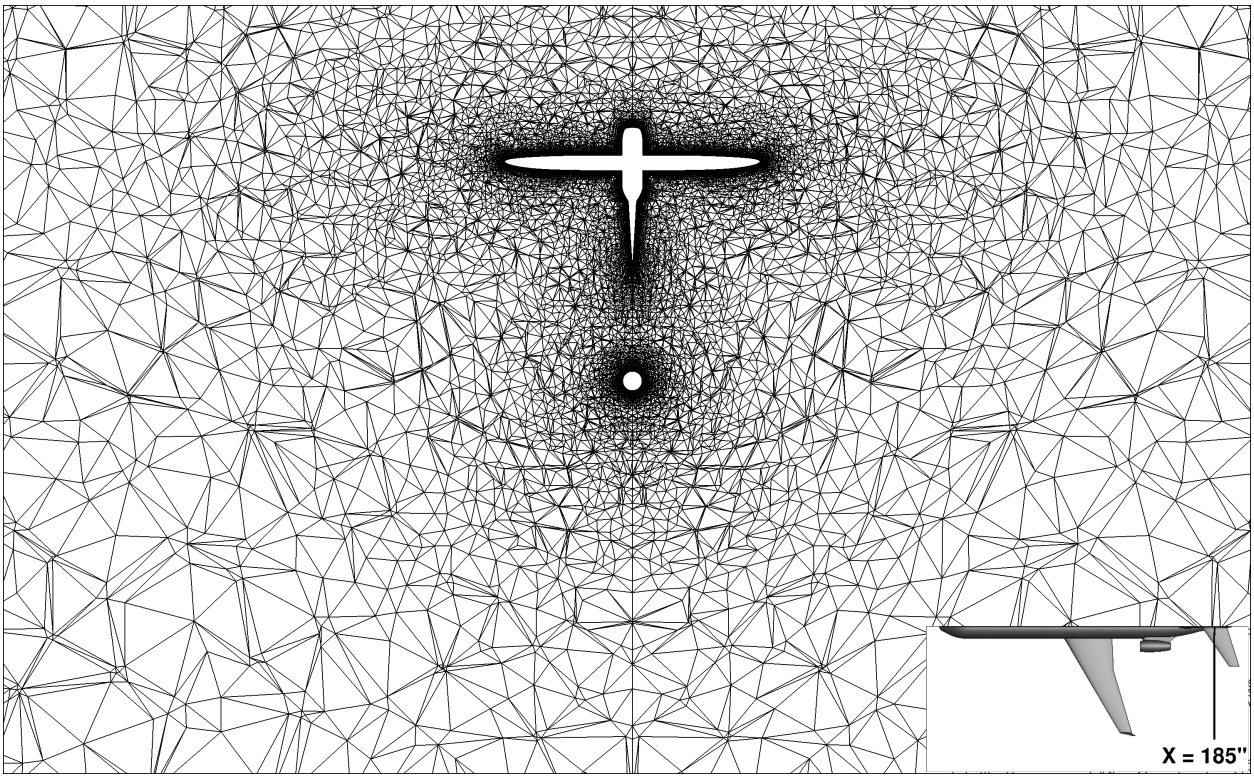

(d) X = 185 inches.

Fig. 3 Concluded

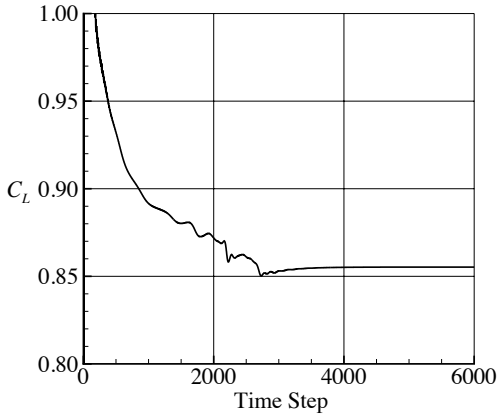

(a) C_L history for Grid 2 at M_∞ = 0.126, α = 10°, and $Re_{\bar{c}} = 0.27 \times 10^6$.

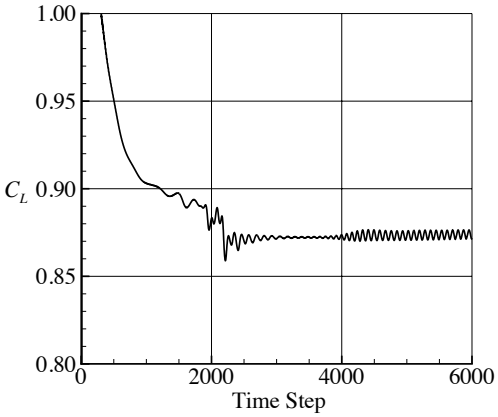

(b) C_L history for Grid 2 at M_∞ = 0.126, α = 11°, and $Re_{\bar{c}} = 0.27 \times 10^6$.

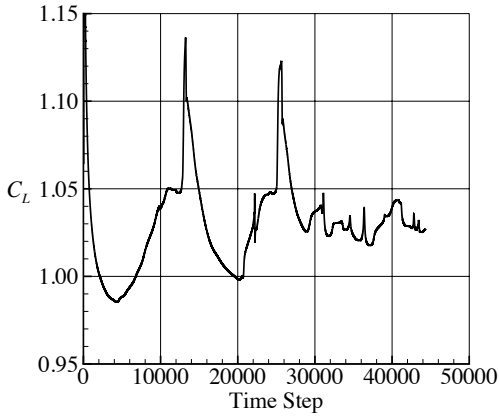

(c) C_L history for Grid 4 at M_∞ = 0.27, α = 16°, and $Re_{\bar{c}} = 16 \times 10^6$.

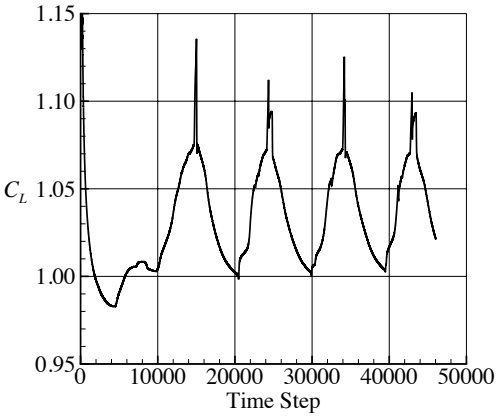

(d) C_L history for Grid 4 at M_∞ = 0.27, α = 17°, and $Re_{\bar{c}} = 16 \times 10^6$.

Fig. 4 Four examples of the C_L convergence history.

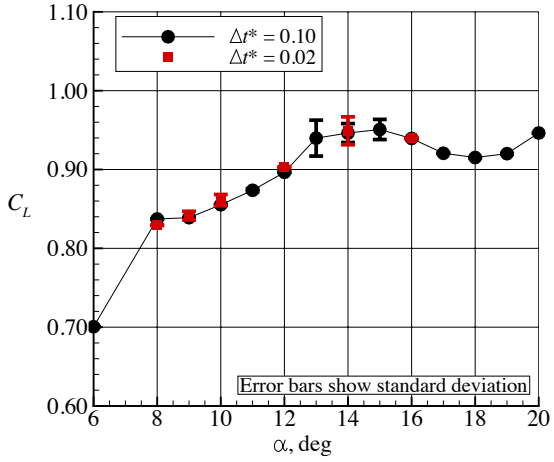

(a) C_L vs. α.

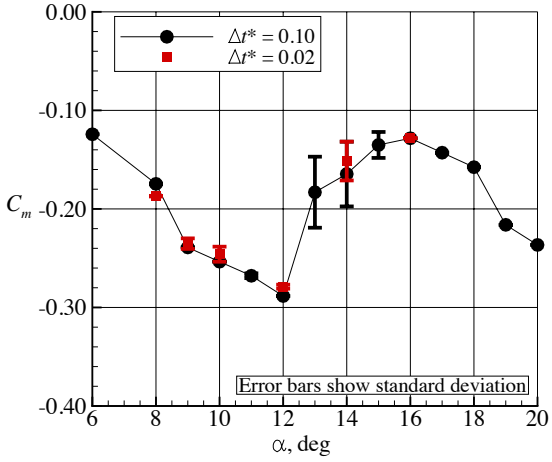

(b) C_m vs α.

Fig. 5 Effect of Δt^* on the aerodynamic coefficients for Grid 2 at M_∞ = 0.126, $Re_{\bar{c}} = 0.27 \times 10^6$, and 6° $\leq \alpha \leq$ 20° using the SA turbulence model.

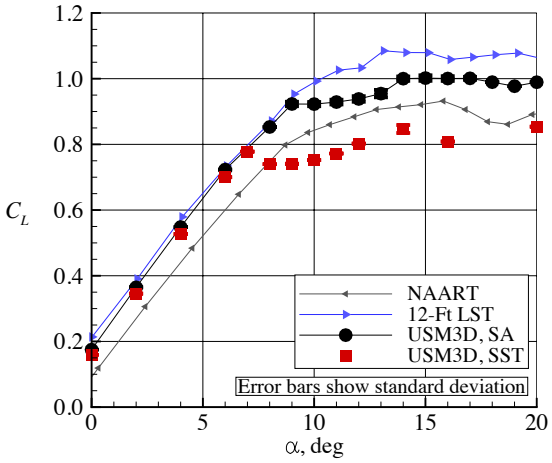

(a) Lift characteristics, C_L vs. α.

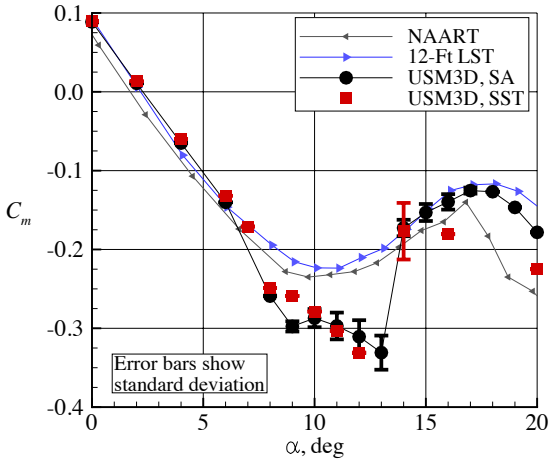

(b) Pitching moment characteristics, C_m vs α.

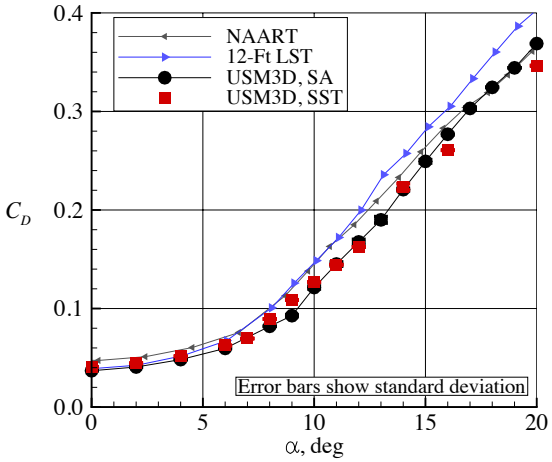

(c) Drag characteristics, C_D vs α.

This space intentionally left blank.

Fig. 6 Effect of turbulence model on the aerodynamic coefficients for Grid 3 at M_∞ = 0.126, $Re_{\bar{c}}$ = 1.6×10^6, and $0° \leq \alpha \leq 20°$ using Δt^* = 0.02.

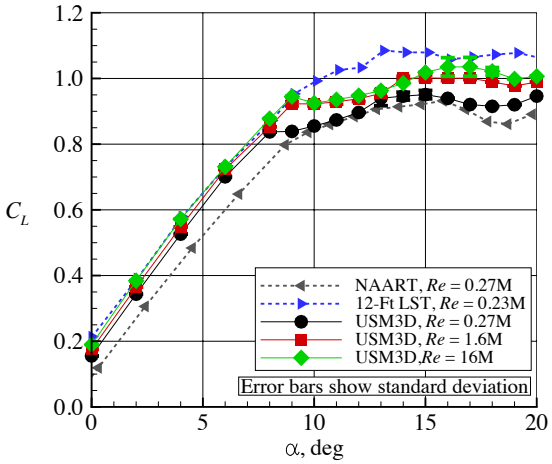

(a) Lift characteristics, C_L vs. α.

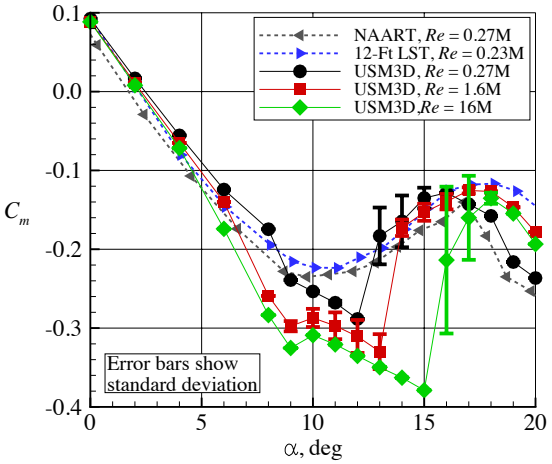

(b) Pitching moment characteristics, C_m vs α.

Fig. 7 Effect of Reynolds number on the aerodynamic coefficients at $0° \leq \alpha \leq 20°$.

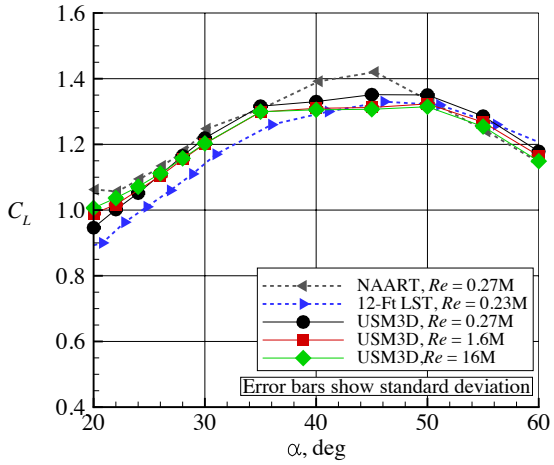

(a) Lift characteristics, C_L vs. α.

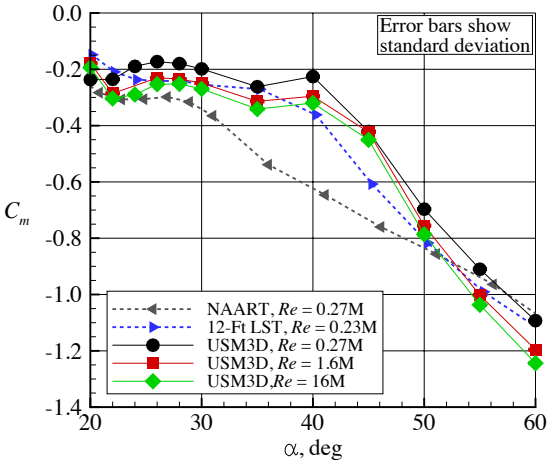

(b) Pitching moment characteristics, C_m vs α.

Fig. 8 Effect of Reynolds number on the aerodynamic coefficients at $20° \leq \alpha \leq 60°$.

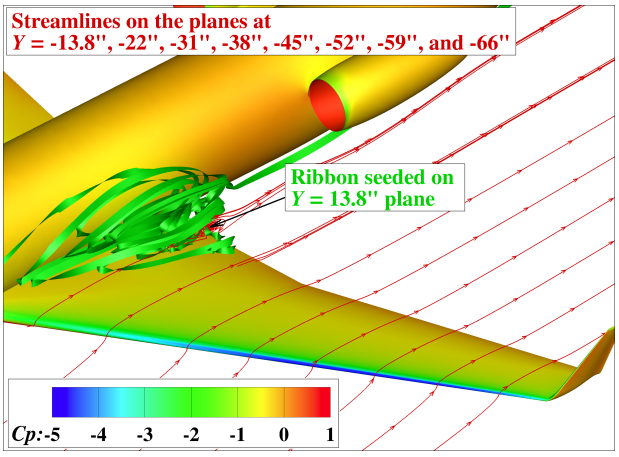

(a) α = 9°.

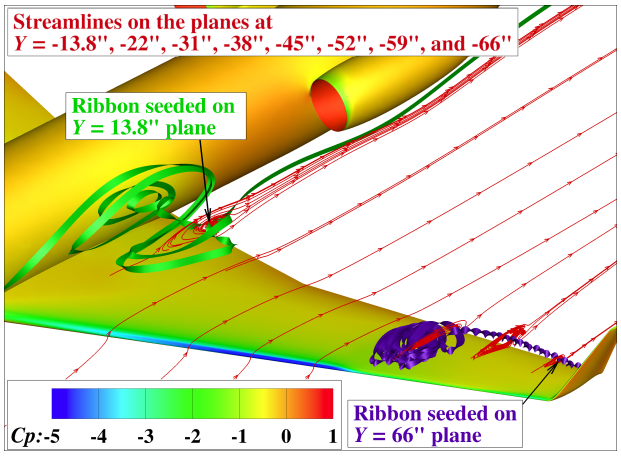

(b) α = 10°.

Fig. 9 Surface C_p contours and streamline data for α = 9° and 10° at M_∞ = 0.126 and $Re_{\bar{c}} = 1.6 \times 10^6$.

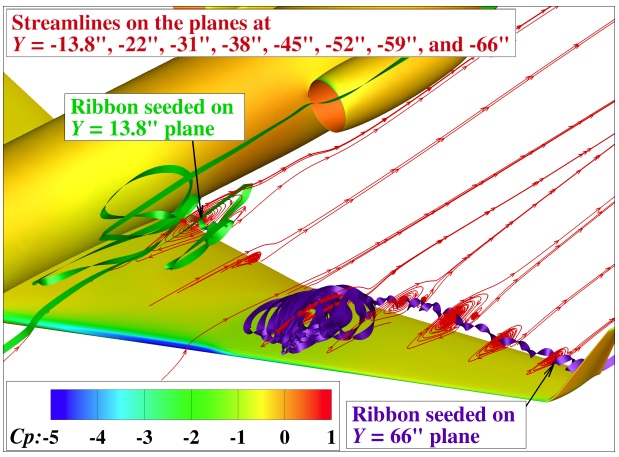

(a) α = 13°.

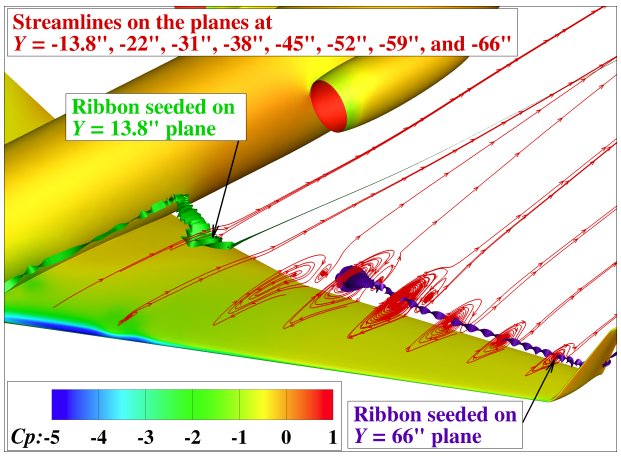

(b) α = 14°.

Fig. 10 Surface C_p contours and streamline data for α = 13° and 14° at M_∞ = 0.126 and $Re_{\bar{c}} = 1.6 \times 10^6$.

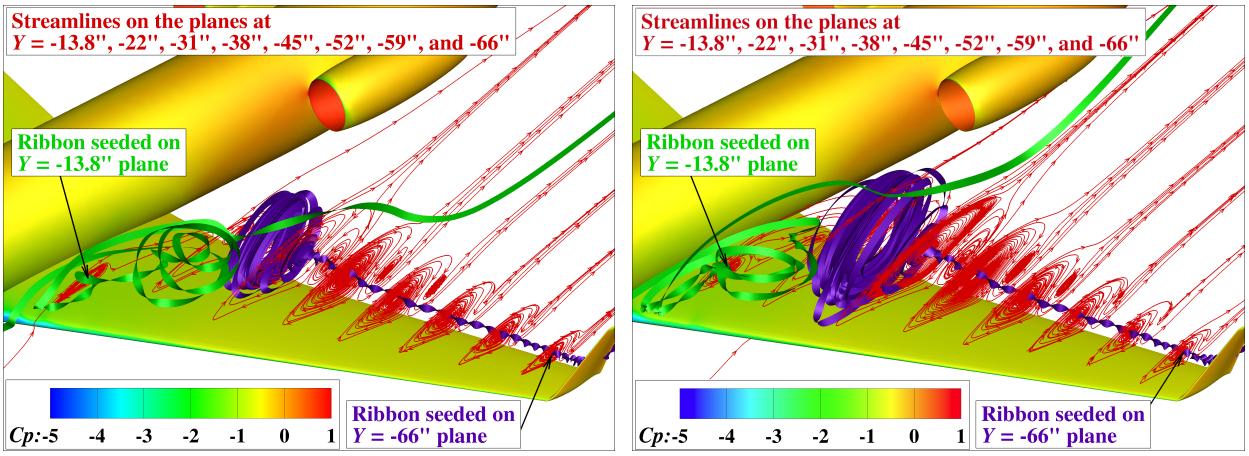

(a) α = 18°. **(b) α = 19°.**

Fig. 11 Surface C_p contours and streamline data for α = 18° and 19° at M_∞ = 0.126 and $Re_{\bar{c}} = 1.6 \times 10^6$.

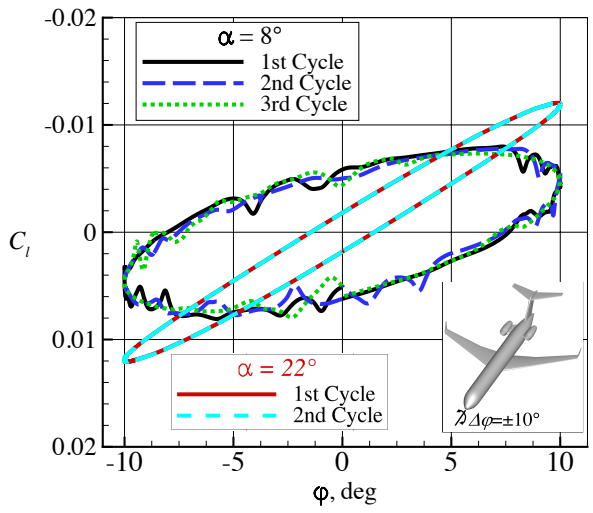

Fig. 12 C_l hysteresis data from USM3D roll forced-oscillation solutions for Grid 4 at α = 8° and 22°, M_∞ = 0.27, $Re_{\bar{c}} = 16 \times 10^6$, and k_R = 0.0940.

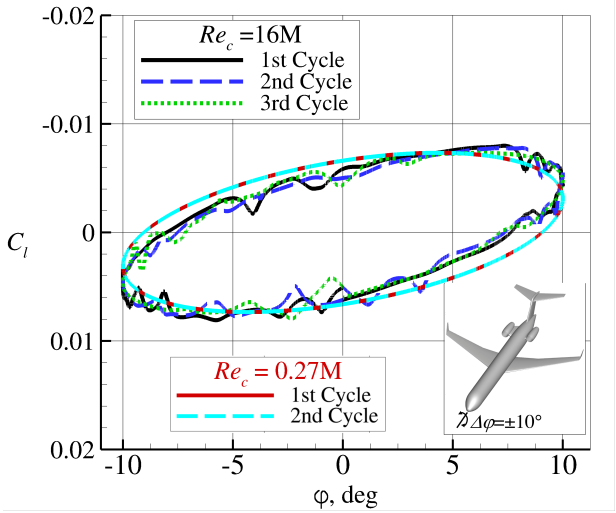

Fig. 13 C_l hysteresis data from USM3D roll forced-oscillation solutions at $Re_{\bar{c}} = 0.27 \times 10^6$ and 16×10^6, M_∞ = 0.27, and α = 8°.

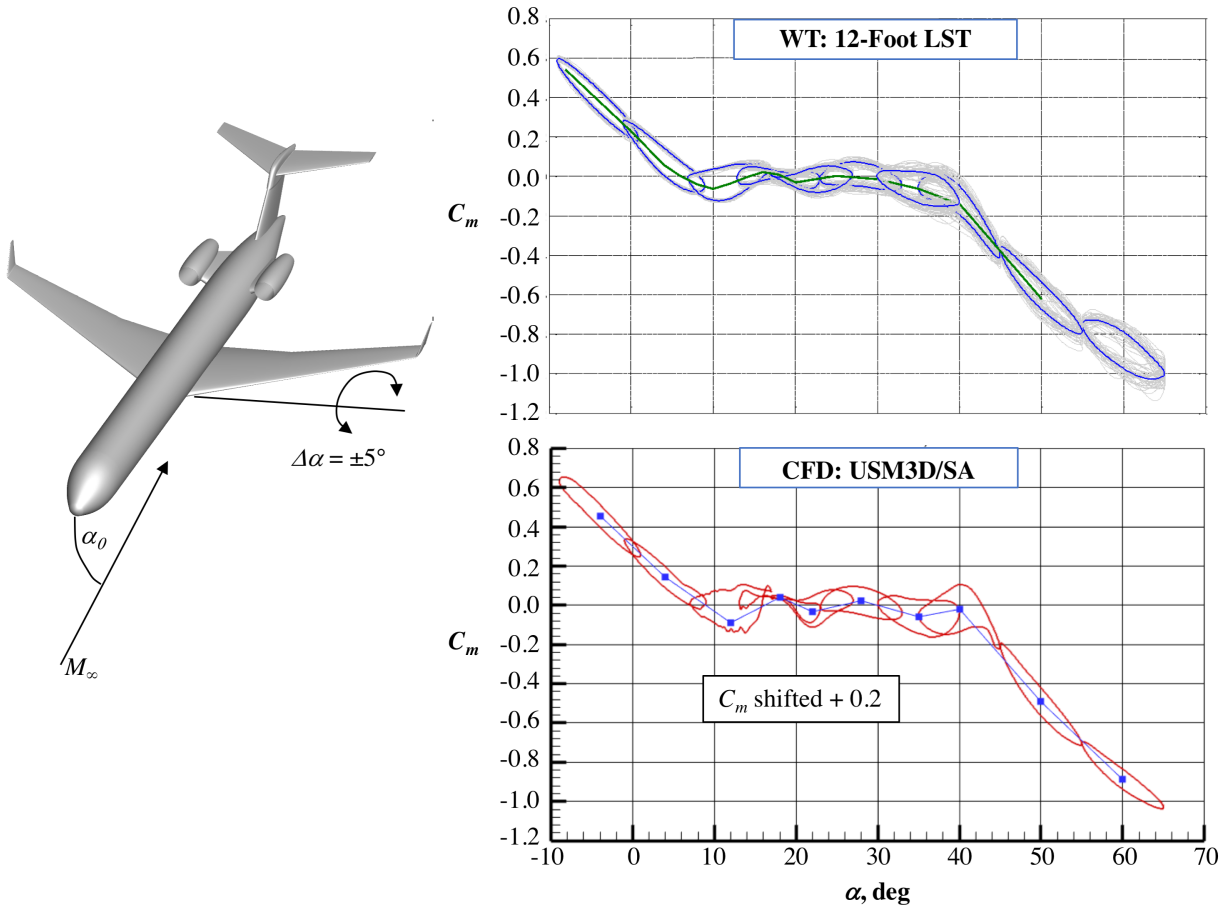

Fig. 14 Comparison of C_m between the USM3D pitch F-O solutions and experimental data at k_P = 0.0158 and low $Re_{\bar{c}}$.

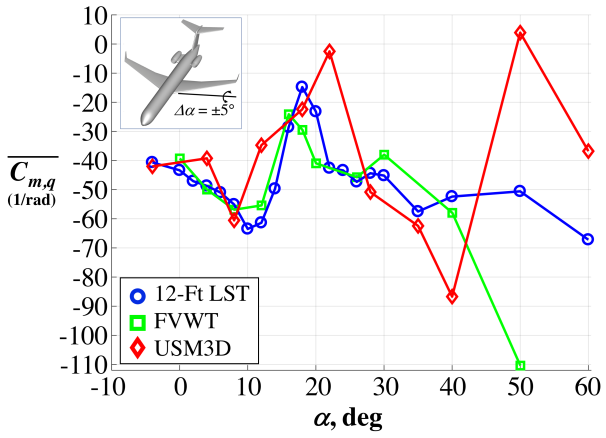

Fig. 15 Comparison of the USM3D pitch damping coefficient with experimental data at k_P = 0.0158 and low $Re_{\bar{c}}$.

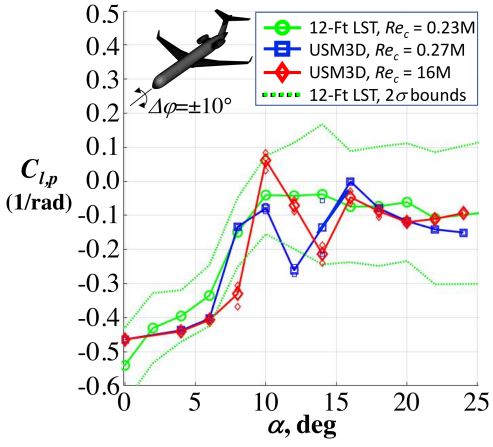

Fig. 16 Effect of $Re_{\bar{c}}$ on the USM3D roll damping coefficient and comparison to experimental data at k_R = 0.094.

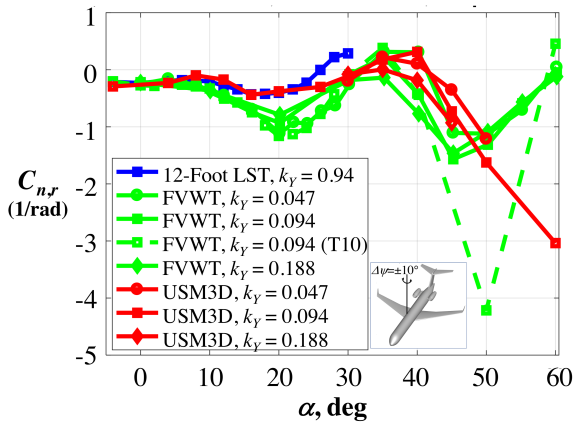

Fig. 17 Effect of k_Y on the USM3D and experimental yaw damping coefficient at low $Re_{\bar{c}}$.

This space intentionally left blank.

References

[1] Belcastro, C., and Foster, J., "Aircraft loss-of-control accident analysis," *AIAA Paper 2010-8004*, 2010.

[2] Shah, G. H., Cunningham, K., Foster, J. V., Fremaux, C. M., Stewart, E. C., Wilborn, J. E., Gato, W., and Pratt, D. W., "Wind-tunnel investigation of commercial transport aircraft aerodynamics at extreme flight conditions," Tech. rep., SAE Technical Paper, 2002.

[3] Foster, J., Cunningham, K., Fremaux, C., Shah, G., Stewart, E., Rivers, R., Wilborn, J., and Gato, W., "Dynamics modeling and simulation of large transport airplanes in upset conditions," *AIAA Paper 2005-5933*, 2005.

[4] Wilborn, J., and Foster, J., "Defining commercial transport loss-of-control: A quantitative approach," *AIAA Paper 2004-4811*, 2004.

[5] "Qualification, Service, and Use of Crewmembers and Aircraft Dispatchers; Final Rule, 14 CFR Part 121," *Federal Aviation Administration, Federal Register, Vol 78, No. 218, Nov. 12, 2013*, 2013. URL: http://www.gpo.gov/fdsys/pkg/FR-2013-11-12/pdf/2013-26845.pdf.

[6] Frink, N. T., Murphy, P. C., Atkins, H. L., Viken, S. A., Petrilli, J. L., Gopalarathnam, A., and Paul, R. C., "Computational Aerodynamic Modeling Tools for Aircraft Loss of Control," *Journal of Guidance, Control, and Dynamics*, Vol. 40, No. 4, 2016, pp. 789–803.

[7] Cunningham, K., Shah, G. H., Frink, N. T., McMillin, S. N., Murphy, P. C., Brown, F. R., Hayes, P. J., Shweyk, K. M., and Nayan, S. N., "Preliminary Test Results for Stability and Control Characteristics of a Generic T-tail Transport Airplane at High Angle of Attack," *AIAA 2018-0529*, 2018.

[8] Cunningham, K., Murphy, P. C., Gautam H. Shah, M. A. H., and Pickering, B. P., "Flight Dynamics Modeling for Stall Training," *57th AIAA Aerospace Sciences Meeting*, AIAA, 2019.

[9] Frink, N. T., Pirzadeh, S. Z., Parikh, P. C., Pandaya, M. J., and Bhat, M. K., "The NASA Tetrahedral Unstructured Software System (TetrUSS)," *Aeronattical Journal*, Vol. 104, No. 1040, 2000, pp. 491–499.

[10] Murphy, P. C., Frink, N. T., McMillin, S. N., Cunningham, K., and Shah, G. H., "Unsteady Model Estimation for Generic T-Tail Transport Aircraft Using Computational Data," *57th AIAA Aerospace Sciences Meeting*, AIAA, 2019.

[11] Frink, N. T., Hiller, B. R., Murphy, P. C., Cunningham, K., and Shah, G. H., "Investigation of Reduced-Order Modeling for Aircraft Stability and Control Prediction," *57th AIAA Aerospace Sciences Meeting*, AIAA, 2019.

[12] Kuehme, D., Alley, N. R., Phillips, C., and Cogan, B. R., "Flight Test Evaluation and System Identification of the Area-I Prototype-Technology-Evaluation Research Aircraft (PTERA)," *AIAA 2014-2577*, 2014.

[13] Belcastro, C. M., Foster, J. V., Shah, G. H., Gregory, I. M., and Cox, D. E., "Aircraft Loss of Control Problem Analysis and Research Toward a Holistic Solution," *Journal of Guidance, Control, and Dynamics*, Vol. 40, No. 4, 2017, pp. 733–775.

[14] Pirzadeh, S., "Three-Dimensional Unstructured Viscous Grids by the Advancing Layer Method," *AIAA Journal*, Vol. 33, No. 1, 1996, pp. 43–49.

[15] Pirzadeh, S., "Advanced Unstructured Grid Generation for Complex Aerodynamic Applications," *AIAA Journal*, Vol. 48, No. 5, 2010, pp. 904–915.

[16] Frink, N. T., "Tetrahedral Unstructured Navier-Stokes Method for Turbulent Flows," *Aeronattical Journal*, Vol. 36, No. 11, 1998, pp. 1975–1982.

[17] Pandya, M., Frink, N. T., Abdol-Hamid, K. S., Samareh, J. A., Parlette, E. B., and Taft, J. R., "Enhancements to TetrUSS for NASA Constellation Program," *Journal of Spacecraft and Rockets*, Vol. 49, No. 4, 2012, pp. 617–631.

[18] Thompson, J. R., Frink, N. T., and Murphy, P. C., "Guidelines for Computing Longitudinal Dynamic Characteristics of a Subsonic Transport," *AIAA 2010-4819*, 2010.